Lifting the Spin-Momentum Locking in Ultra-Thin Topological Insulator Films

Arthur Leis, Michael Schleenvoigt, Vasily Cherepanov, Felix Lüpke, Peter Schüffelgen, Gregor Mussler, Detlev Grützmacher, Bert Voigtländer,* and F. Stefan Tautz

3D topological insulators are known to carry 2D Dirac-like topological surface states in which spin-momentum locking prohibits backscattering. When thinned down to a few nanometers, the hybridization between the topological surface states at the top and bottom surfaces results in a topological quantum phase transition, which can lead to the emergence of a quantum spin Hall phase. Here, the thickness-dependent transport properties across the quantum phase transition are studied on the example of $(Bi_{0.16}Sb_{0.84})_2Te_3$ films, with a four-tip scanning tunneling microscope. The findings reveal an exponential drop of the conductivity below the critical thickness. The steepness of this drop indicates the presence of spin-conserving backscattering between the top and bottom surface states, effectively lifting the spin-momentum locking and resulting in the opening of a gap at the Dirac point. The experiments provide a crucial step toward the detection of quantum spin Hall states in transport measurements.

1. Introduction

Since the discovery of 3D topological insulators (TIs),[1–4] an increasing number of novel topological phases have been realized. For example, in magnetically doped 3D TI thin films, a quantum anomalous Hall (QAH) phase with 1D chiral edge states was reported.[5–7] More recent examples are co-existing QAH and axion insulator phases in a stoichiometric magnetic topological insulator.[8,9] The emergence of these exotic topological phases is underpinned by the breaking of time-reversal symmetry, which opens a gap at the Dirac point and leads to massive Dirac fermions. Yet another possibility to gap out the Dirac point of a 3D TI is to reduce its thickness below a critical value at which the topological surface states (TSS) at the top and bottom of the film start to interact. In the prototypical 3D TI $(Bi_{1-x}Sb_x)_2Te_3$ (BST), this occurs at thicknesses below $\simeq 5$ quintuple layers (QL).

While 180°-backscattering of electrons in the TSS is prohibited by spin-momentum locking as long as the states on opposite surfaces are strictly separated,[10] spin-conserving backscattering becomes possible if opposite TSS interact and electrons are able to scatter from the top to the bottom surface and vice versa, as illustrated in **Figure 1**a. In such ultra-thin TI films, a quantum spin Hall (QSH) phase with 1D helical edge states is predicted to emerge.[11–14] Intuitively, the latter can be understood as a remnant of the 2D TSS on the side faces of the film, when upon film thinning they are reduced to 1D edges.

Figure 1b indicates that the coupling between opposite TSS in an ultra-thin TI film has two consequences: On the one hand, the band structure will change from two separate Dirac cones to a single gapped structure. Note that the continuity of transport in a loop around the material means that the Dirac cones on the top and bottom surfaces have interchanged spins (Figure 1b, left). Precisely, this allows spin-conserving scattering from k to $-k$ if top and bottom surface states interact (Figure 1b, right), which effectively corresponds to a lifting of spin-momentum locking in the TSS. Therefore, as a second consequence, in addition to the modification of their dispersion, the lifetime of the electrons in the surface states is expected to drop. While the gap opening at the Dirac point has been detected in angle-resolved photoemission spectroscopy and scanning tunneling spectroscopy experiments on ultra-thin TI films,[15–17] the second effect has not yet been observed, since it requires the systematic measurement of

A. Leis, V. Cherepanov, F. Lüpke, B. Voigtländer, F. S. Tautz
Peter Grünberg Institut (PGI-3)
Forschungszentrum Jülich
Jülich 52425, Germany
E-mail: b.voigtlaender@fz-juelich.de
A. Leis, M. Schleenvoigt, V. Cherepanov, F. Lüpke, P. Schüffelgen,
G. Mussler, D. Grützmacher, B. Voigtländer, F. S. Tautz
Jülich Aachen Research Alliance (JARA)
Fundamentals of Future Information Technology
Jülich 52425, Germany
A. Leis, B. Voigtländer, F. S. Tautz
Experimentalphysik IV A
RWTH Aachen University
Otto-Blumenthal-Straße
Aachen 52074, Germany
M. Schleenvoigt, P. Schüffelgen, G. Mussler, D. Grützmacher
Peter Grünberg Institut (PGI-9)
Forschungszentrum Jülich
Jülich 52425, Germany

**ADVANCED
SCIENCE NEWS**
www.advancedsciencenews.com

**ADVANCED
QUANTUM
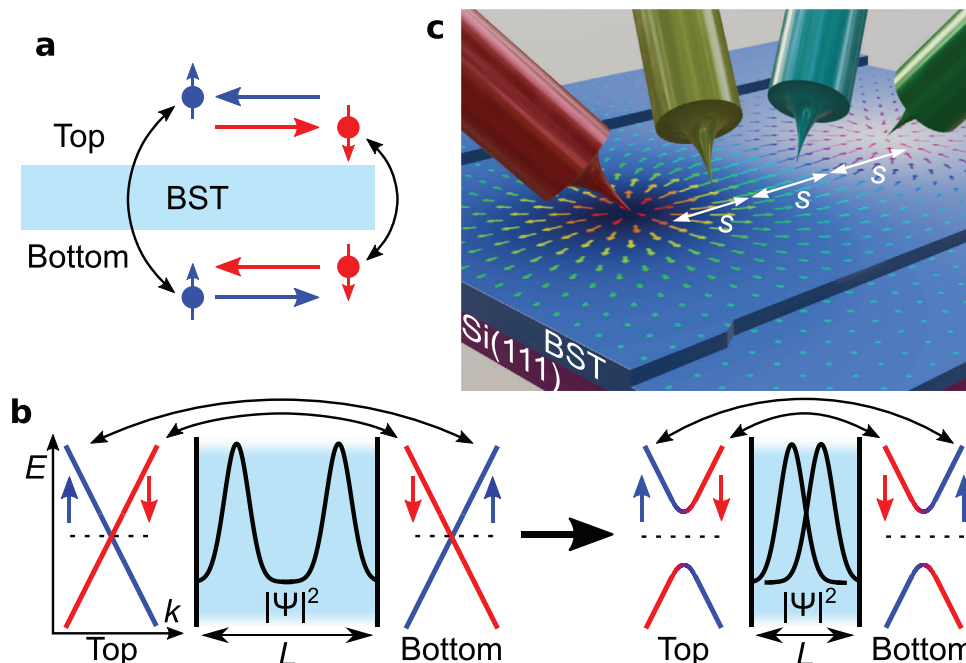TECHNOLOGIES**
www.advquantumtech.com

Figure 1. Scheme of the multi-tip STM experiment to detect scattering between topological surface states. a) Scattering between topological surface states at the top and the bottom surfaces of a $(Bi_{1-x}Sb_x)_2Te_3$ thin film with thickness L below a critical value of 5 QL. b) Because of the hybridization of the overlapping wave functions of both topological surface states, a gap opens at the Dirac point. Hybridization also enables spin-conserving scattering from k to $-k$. c) Experimental setup. The boundary region of the BST film forms a wedge with step heights of single quintuple layers. Positioning the tips of a four-tip STM on a single terrace allows measuring the sheet conductivity σ as a function of the film thickness L. The arrows in the sketch indicate current flow.

the transport properties of pristine samples, which is difficult in lithographically patterned samples, because the processing tends to degrade the ultra-thin films. For this reason, we apply here the methodology of multi-tip scanning tunneling microscopy (STM) as a "multimeter on the nanoscale" to study $(Bi_{1-x}Sb_x)_2Te_3$ films in situ.[18–20]

2. Results and Discussion

Samples are prepared by molecular beam epitaxy (MBE) with a shadow mask, which allows the deposition of a $(Bi_{1-x}Sb_x)_2Te_3$ wedge in which the film thickness increases in steps of single quintuple layers, as suggested conceptually in Figure 1c, from 1 QL $\simeq$ 1 nm at the edge of the film to 12 QL in its center (see Experimental Section for details). We have chosen a stoichiometry of $x = 0.84$, because for this value the Fermi level in the bulk of the film is located in the bulk band gap close to the Dirac point, which reduces parasitic charge transport through the interior of the film.[21,22] Large-scale STM scans at the edge of the film show the step-wise increase of the film thickness (**Figure 2**a) from the Si(111) substrate. For the transport measurements, the four tips are individually navigated into the boundary region of the film, as monitored with an optical microscope (Figure 2b). To measure the local conductivity of the TI film, the four STM tips are positioned in a linear configuration on a single terrace, with distances of $s \simeq 250$ nm between adjacent tips (Figure 2c). In this configuration, the four-point resistance

is measured, from which the 2D sheet conductivity σ can be calculated (see Experimental Section for details). Topography scans demonstrate that the film surface, including the local terrace structure, is still intact after the electrical measurements. Thus, our experiments yield sheet conductivities for well-defined film thicknesses L.

The sheet conductivity displays an exponential increase from 1 QL to 5 QL (**Figure 3**a). Note that for $L > 5$ QL, it is not possible to realize the four-point measurement on a single terrace, because the terraces are too narrow to reliably place the four tips on them. However, large-scale conductivity measurements far away from the film edge with a tip spacing of $s = 50\,\mu$m yield, within measurement error, the same conductivity for the 12 QL interior of the film as for the 5 QL terrace. This saturation of the thickness-dependent conductivity verifies that the TSS at the top and bottom of the film dominate the charge transport. A possible parasitic contribution from bulk states would result in a linear dependence of the conductivity on the film thickness L. We identify the thickness of 5 QL as the film thickness below which the surface states of the two interfaces start to interact noticeably. We note that at this stage (at the latest), the distinction between bulk and surface states will have become obsolete.

According to the Drude model, the sheet conductivity σ is given by carrier concentrations n and carrier mobilities μ in the top and bottom TSS,

$$\sigma = e\left[\mu_t n_t(\Delta, E_{F,t}) + \mu_b n_b(\Delta, E_{F,b})\right] \qquad (1)$$

**ADVANCED
SCIENCE NEWS**

www.advancedsciencenews.com

**ADVANCED
QUANTUM
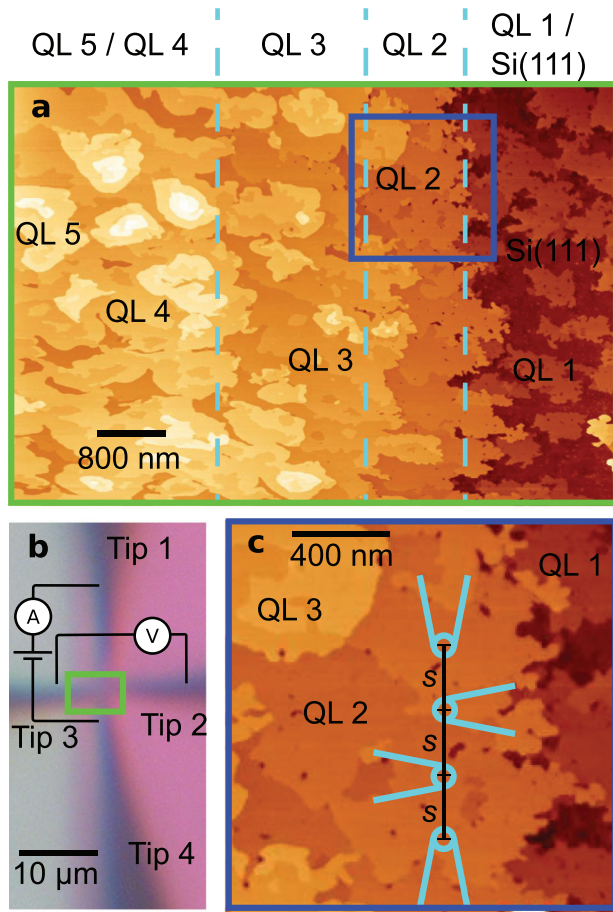TECHNOLOGIES**

www.advquantumtech.com

Figure 2. Measurement configuration and tip positioning method. a) A large overview STM scan is performed with one of the tips to map the topography of the TI film boundary region, as indicated by the green rectangle. This large overview scan serves as a reference map to place all four tips on a single terrace. In the entire overview area, single steps of QL-height are seen, revealing the wedge-shaped structure of the film boundary region. b) Optical microscope image of the final tip configuration. c) The tips are navigated to the desired positions using a method of overlapping STM scans.[26] The tip positions are located by identifying the same topographic features in the small scans and in the overview scan.

where e is the elementary charge. Apart from the Fermi energy E_F, which we consider relative to the Dirac point,[22] and which – due to the presence of the substrate – may differ between the top and bottom surfaces of the film, it is the gap Δ in the topological surface state at the Dirac point that predominantly determines n_t and n_b, through the dispersion relation

$$E(k, L) = \pm \sqrt{[\hbar k v_F]^2 + [\Delta(L)/2]^2} \qquad (2)$$

of the massive Dirac fermions in the vicinity of the Γ-point.[11,23] $\Delta(L)$ has been measured spectroscopically on Sb_2Te_3,[16] yielding the opening of a gap below 5 QL that increases up to a value of $\Delta \simeq 250$ meV for 2 QL, in agreement with theoretical predictions.[14] Since our sample has similar composition, we use these values for $\Delta(L)$. v_F is the Fermi velocity, which determines the slope of the Dirac cone and therefore does not depend on the film thickness. We use a value of $v_F = 4.2 \times 10^5$

ms^{-1}, as measured in a previous photoemission study on samples of identical composition and confirmed by an interpolation (see Experimental Section).[24] Before we can determine σ, we still need the Fermi levels. While $E_{F,t}$ is accessible through photoemission experiments, $E_{F,b}$ follows from gate-dependent transport experiments (see Supporting Information). For the present sample, we find $E_{F,t} \simeq 50$ meV and $E_{F,b} \simeq -50$ meV for $L \geq 5$ QL (see Experimental Section). In principle, substrate interaction can also introduce asymmetries between the top and the bottom surface of the TI film regarding spin-momentum locking. However, in our model, we only allow for different positions of the Fermi level and different carrier mobilities at the top and bottom interfaces in the form of three open parameters, but assume no further effect of the substrate, because in the investigated sample system the substrate is separated from the TI film by the van der Waals gap and a tellurium passivation layer (see Experimental Section), which help to electronically decouple the film from the underlying silicon.

With these parameters, we can calculate the expected sheet conductivities for different L from Equation (1) under the assumption that n_t, n_b, μ_b and μ_t change due to the gap opening, in particular μ_t, according to

$$\frac{\mu_t(L)}{\mu_t(L')} = \frac{m_t^*(L')}{m_t^*(L)} = v_F^2 \frac{m_t^*(L')}{\sqrt{E_{F,t}^2 + [\Delta(L)/2]^2}} \qquad (3)$$

where $m^*(L)$ is the thickness-dependent effective carrier mass (see Experimental Section). Here, the electron mobility $\mu_t = e\tau_0/m^*$ at the top of the film changes only through the change in the band structure associated with the gap opening and the resulting change in effective mass m^*, while the scattering time τ_0 stays fixed. In addition, we assume a ratio r_μ between the top and bottom mobilities. The minimum sheet conductivities $\sigma(L)$ predicted by this model (see Experimental Section for details) for $L' = 5$ QL are displayed as black dots in Figure 3a. For this purpose, the global minima of the model conductivity are determined from variation of the three open parameters within reasonable ranges of $E_{F,t}$, $E_{F,b} \in [-50 \text{ meV}; 50 \text{ meV}]$, and $r_\mu \in [0.3; 1]$. This is shown exemplary for $E_{F,t}$ in Figure 3b. We find that this model cannot explain the sharp drop of the experimentally determined sheet conductivity. Finding the global minima of the calculated conductivity to be larger than the experimentally observed values in the range of the three open parameters, we therefore conclude that the measured thickness-dependent conductivity drops too sharply to be explained by a mere band structure effect, assuming gap values of $\Delta(2 \text{ QL}) \simeq 250$ meV, $\Delta(3 \text{ QL}) \simeq 60$ meV, $\Delta(4 \text{ QL}) \simeq 25$ meV from scanning tunneling spectroscopy.[16]

If a new efficient scattering channel appears at small film thicknesses $L < 5$ QL, Matthiesen's rule $\tau^{-1} = \tau_0^{-1} + \tilde{\tau}^{-1}$ predicts a decrease in the overall scattering time τ, which could explain the sharp drop in the sheet conductivity by a corresponding drop in the mobility. In fact, once the top and bottom surface states interact, we expect the emergence of inter-TSS scattering $\tilde{\tau}$, in addition to the intra-TSS scattering τ_0 which originates from surface (or interface) defects and the electron–phonon interaction. Including this additional scattering mechanism in our model, we
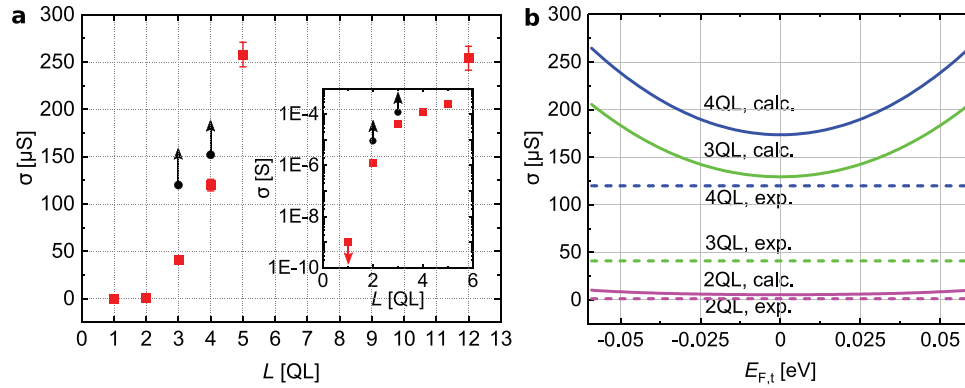
**ADVANCED
SCIENCE NEWS**
www.advancedsciencenews.com

**ADVANCED
QUANTUM
TECHNOLOGIES**
www.advquantumtech.com

Figure 3. Measured thickness-dependent sheet conductivity compared to calculations based on the TSS band structure. a) Thickness-dependent conductivity (red squares with error bars) as obtained from four-point measurements on single terraces of different layer thickness in the TI film. The minimum of the calculated conductivity, obtained when varying $E_{F,t}$, $E_{F,b} \in [-50\,\text{meV}; 50\,\text{meV}]$, and $r_\mu \in [0.3; 1]$, is indicated by black dots. The inset shows a logarithmically scaled plot of the same data. b) Calculated conductivity as function of $E_{F,t}$, with $r_\mu = 1$ and $E_{F,b} = -50\,\text{meV}$ (Equation (1)).
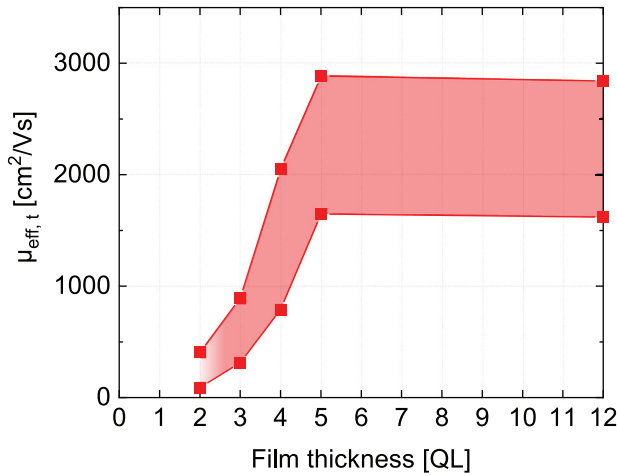

Figure 4. Thickness-dependent electron mobility as inferred from experimental results. For $L \leq 4$ QL, the mobility $\mu_{\text{eff,t}}$ is the mobility in the coupled top and bottom TSS. It is reduced below the value for $L \geq 5$ QL by the lifting of the spin-momentum locking in ultra-thin films, as effected by the onset of of spin-conserving 180°-backscattering between the top and the bottom surfaces of the film (inter-TSS scattering). For $L \geq 5$ QL, the mobility $\mu_{\text{eff,t}}$ corresponds to the electron mobility in the top TSS, limited by intra-TSS scattering only. The band indicated in red represents the range of mobility values obtained for the range of the parameters $E_{F,t}$, $E_{F,b,}$ and r_μ discussed in the main text and the Experimental Section. The corresponding inter-TSS scattering times are 11 fs < $\tilde{\tau}_{4\text{QL}}$ < 56 fs, 10 fs < $\tilde{\tau}_{3\text{QL}}$ < 19 fs, and 8 fs < $\tilde{\tau}_{2\text{QL}}$ < 45 fs. For $L \geq 5$ QL, $E_{F,t}$ is known and the red band is influenced only by r_μ and $E_{F,b}$.

obtain from the experimental data in Figure 3a the effective electron mobility in the top TSS according to Matthiesen's rule

$$\mu_{\text{eff,t}}(L) = \frac{\mu_t(L)\tilde{\mu}_t(L)}{\mu_t(L) + \tilde{\mu}_t(L)} \quad (4)$$

being composed of the intra-TSS mobility μ_t and the inter-TSS mobility $\tilde{\mu}_t$, depending on the three parameters $E_{F,t}$, $E_{F,b}$, and r_μ for the different film thicknesses L (**Figure 4**). Details on the determination of the total mobility from the experimental

values are found in the Experimental Section. Because the parameters $E_{F,t}$, $E_{F,b}$, and r_μ are not known, it is only possible to display a band within which the mobility $\mu_{\text{eff,t}}$ must lie. More specifically, the limits displayed in Figure 4 are obtained from finding the global maximum/minimum of the mobility from the experimentally observed sheet conductivity upon variation of $E_{F,t}$, $E_{F,b} \in [-50\,\text{meV}; 50\,\text{meV}]$, and $r_\mu \in [0.3; 1]$ for each film thickness. In doing so, the parameters $E_{F,t}$ and $E_{F,b}$ are found to have the strongest influence on the limits. The plot shows a dramatic decrease of the total mobility of the top surface $\mu_{\text{eff,t}}$. This decrease explains the deviation between experimental and calculated data points in Figure 3a. Regarding the strength of the inter-TSS scattering, we find that $\tilde{\tau} < \tau_0$ for all thicknesses 2 QL $\leq L \leq$ 4 QL, that is, the inter-layer scattering dominates the intra-layer scattering. For 2 QL, τ_0 is between two and eight times larger than $\tilde{\tau}$, and values for $\tilde{\tau}$ range between approximately 10 and 50 fs. We also find that the dependence of $\tilde{\tau}$ on L is weak, as 11 fs < $\tilde{\tau}_{4\text{QL}}$ < 56 fs, 10 fs < $\tilde{\tau}_{3\text{QL}}$ < 19 fs, and 8 fs < $\tilde{\tau}_{2\text{QL}}$ < 45 fs. This can be rationalized as a compound effect of an increasing matrix element for scattering as a result of rising wave function overlap on the one hand, and a decreasing density of states at the Fermi level to scatter into as the band gap opens on the other hand.

3. Conclusion

In conclusion, using the BST sample system, we deduce that in ultra-thin films of 3D topological insulators, the scattering between topological surface states on opposite faces of the film significantly reduces the sheet conductivity beyond what is expected from the opening of a Dirac gap alone. This inter-TSS scattering is in fact the dominant scattering mechanism, because the interaction of top and bottom surface states effectively lifts the spin-momentum locking and spin-conserving 180°-backscattering becomes possible between the top to the bottom surface state, thus opening an additional scattering channel (Figure 1a). So far, our modeling of the four-tip transport data requires us to employ several parameters from spectroscopic measurements on similar samples. Currently, we are constructing a four-tip STM that will allow magnetoconductance and Hall measurements at low temperatures, which for future transport

**ADVANCED
SCIENCE NEWS**

www.advancedsciencenews.com

**ADVANCED
QUANTUM
TECHNOLOGIES**

www.advquantumtech.com

studies will provide experimental access to all necessary sample parameters, thereby eliminating the need to use parameters from spectroscopic experiments. Additionally, potentiometry measurements can offer further microscopic information on transport in topological insulator films.[19,25]

Even if the Fermi level is not located in the hybridization gap Δ and the influence of the gap on the transport is hence expected to be small, the additional inter-TSS scattering decreases the surface state conductivity. This effect helps to establish an insulating 2D interior against which 1D edge states, for example, in a QSH phase, prevail. A requirement for the actual measurement of 1D edge channels in transport measurements is that the edge state conductivity is not overwhelmed by a large parasitic 2D conductivity. The 2D conductivity we have found in the studied ultrathin TI films is sufficiently small to disentangle this parasitic contribution from the auspicious 1D edge state conductivity in future experiments. Experiments with multi-tip STM on pristine surfaces on the sub-µm scale are thus an important step toward the detection and characterization of possible 1D edge states in transport measurements.

4. Experimental Section

Sample Preparation: The $(Bi_{0.16}Sb_{0.84})_2Te_3$ thin films were grown on a silicon-on-insulator (SOI) substrate, the latter consisting of a degenerately doped Si(100) handle wafer, a 300 nm oxide layer, and an undoped 70 nm Si(111) template layer. Employing a thin intrinsic Si layer as template for growth reduces the substrate sheet conductivity in the experiments to $\simeq 2$ nS.

The substrate was cleaned by Piranha solution (H_2SO_4:H_2O_2 2:1) and an HF (1%) dip to remove organic contaminations and native oxides, respectively, while also supplying a protective hydrogen passivation. After transfer into the MBE chamber (base pressure $p \simeq 1 \times 10^{-9}$ mbar), the substrate was heated to 700 °C for 10 min for hydrogen desorption and subsequently cooled down to 262 °C for growth. Bi, Sb, and Te were evaporated from standard Knudsen effusion cells at temperatures of 440, 470, and 330 °C, respectively, resulting in a flux ratio of 1:20:120. Initially, the substrate was flushed with Te to saturate the Si dangling bonds before supplying Bi and Sb for TI growth, which also helped to decrease the influence of the Si substrate on the electronic structure of the TI.

Growth takes place through a removable shadow mask in order to achieve a TI film with boundaries on the SOI substrate without the need of ex situ processing. In the boundary region of the shadow mask, the thickness of the TI film decreases in steps of single quintuple layers from the maximum film thickness of 12 QL to zero, exposing the Si(111) template layer. Apart from quintuple layer steps of 1 nm height each, substrate steps of 0.3 nm height in the topography (diagonally oriented in Figure 2a) are seen, which are easily distinguishable. Note that counting steps of specific height from the substrate excludes film thickness errors.

Four-Point Transport Measurements: After growth, the sample was transferred in vacuum ($p \leq 1 \times 10^{-9}$ mbar) into the room-temperature four-tip STM (base pressure $p \simeq 4 \times 10^{-10}$ mbar). The vacuum transfer of the sample and the absence of any processing steps after the growth enabled to measure transport properties of the pristine TI film, avoiding any detrimental influence of passivation or lithography steps. Aging effects of the investigated sample in the UHV system were not observed. Even after 4 months of being stored in the system, no changes in surface conductivity were detected and no signs of surface degradation were observed in topography scans.

The STM tips were electrochemically etched tungsten wires. An optical microscope was used to position four STM tips in the boundary region of the $(Bi_{0.16}Sb_{0.84})_2Te_3$ film on the sample (coarse navigation). In the optical microscope, the wedge-shaped boundary region appeared as a blend of colors between grey (12 QL TI film) and pink (Si substrate) (Figure 2c).

After optical coarse positioning, large-scale STM images were recorded to obtain an overview of the topography of the TI film in the corresponding area. Then the STM tips were individually and precisely positioned on a chosen terrace of specific thickness L (which could be determined by counting step edges) in a linear four-point configuration with a distance $s \simeq 250$ nm between the tips. To this end, a positioning method relying on overlapping small-area STM scans, performed successively with each tip, was employed.[26]

Once the four tips were positioned laterally, they were driven from the tunneling regime into contact with the sample surface. In this electrical point contact regime, the sheet conductivity σ of the TI film was measured by repeatedly recording the voltage drop V between the two inner tips as a function of the current I injected between the two outer tips. For each L, experiments were repeated in at least two different areas of the sample (see Supporting Information). In the given contact geometry, the sheet conductivity σ of a 2D film is given by[27]

$$\sigma = \frac{\ln 2}{\pi} \frac{I}{V} \tag{5}$$

With an inter-tip distance s smaller than the distance between the tips and the nearest step edge, conductivity contributions from neighboring terraces were negligible.[28] It is noted that the conductivity of 1 nS measured for $L = 1$ QL is an upper boundary, since the conductivity of the bare Si substrate is of the same order of magnitude ($\simeq 2$ nS).

In the experiment, a maximum current of $I \simeq 1$ µA was applied, resulting in a current density of $\simeq 1$ A m^{-1} between the injection tips. After completion of the electrical measurements, the tips were retracted and the sample area was imaged again with STM. In these images, the contact points of the tips were usually discernible as small spots of typically only $\simeq 1$ nm height (Figure S1, Supporting Information), indicating visually that there was no significant damage done to the thin film, neither by contacting nor by electrical heating due to the applied current.

Sample Characterization: The composition of the $(Bi_{1-x}Sb_x)_2Te_3$ thin film was determined ex situ by means of Rutherford backscattering spectroscopy after the electrical four-point experiments. From these measurements, it was found that the Sb concentration in the sample was $x = 0.84$.

With the exact material composition known, the position of the Fermi level $E_{F,t}$ with respect to the Dirac point as well as the Fermi velocity v_F was determined. To this end, spectroscopic data of samples grown previously in the same MBE system were interpolated. Both parameters are approximately linearly dependent on the Sb concentration between $x = 0.5$ and $x = 1$.[29] In a previous angle-resolved photoemission study, the Fermi level $E_{F,t}$ for a $(Bi_{1-x}Sb_x)_2Te_3$ thin film with $x = 0.94$ was found to be located at the Dirac point, that is, $E_{F,t} \simeq 0$.[24] The corresponding Fermi velocity was determined as $v_F \simeq 3.8 \times 10^5$ ms^{-1}. Another sample grown in the same system with a Sb concentration of $x = 0.47$ had $E_{F,t} \simeq 250$ meV and $v_F \simeq 5.6 \times 10^5$ ms^{-1}.[21] Using these two samples as a reference, $E_{F,t} \simeq 50$ meV and $v_F \simeq 4.2 \times 10^5$ ms^{-1} for the present $(Bi_{0.16}Sb_{0.84})_2Te_3$ sample were obtained.

Calculation of the Charge Carrier Density: The dispersion relation Equation (2) in the vicinity of the Dirac point corresponds to a density of states of

$$D(\Delta(L), E) = \frac{|E|}{2\pi(\hbar v_F)^2} \Theta(|E| - \Delta(L)/2) \tag{6}$$

with the energy measured E relative to the Dirac point and Θ being the Heaviside step function.[23] From the density of states, the charge carrier density was calculated as

$$n(\Delta(L), E_F) = \int_0^\infty D(\Delta(L), E) \left[f_n(E, E_F) + f_p(E, E_F) \right] dE \tag{7}$$

with the Fermi distribution function

$$f_n(E, E_F) = f_p(E, -E_F) = \left(1 + \exp\left(\frac{E - E_F}{k_B T} \right) \right)^{-1} \tag{8}$$

ADVANCED
SCIENCE NEWS

www.advancedsciencenews.com

ADVANCED
QUANTUM
TECHNOLOGIES

www.advquantumtech.com

for electrons (n) and holes (p). The charge carrier density n enters the Drude expression in Equation 1. The TSS gaps $\Delta(2\,\text{QL}) \simeq 250$ meV, $\Delta(3\,\text{QL}) \simeq 60$ meV, and $\Delta(4\,\text{QL}) \simeq 25$ meV were taken from ref. [16] and were measured on pure Sb_2Te_3. These results are in agreement with theoretical predictions.[14]

Modeling the Surface Conductivity: No Inter-TSS Scattering: The mobility in the TSS at the top surface of the film is given by

$$\mu_t(L) = \frac{e}{m^*(L)} \tau_0 \tag{9}$$

where τ_0 is the intra-TSS scattering time due to surface defects and electron-phonon scattering. Because of spin-momentum locking in the TSS, spin-conserving 180°-backscattering events do not contribute to τ_0. Also, τ_0 does not depend on the film thickness L, since the primary sources of intra-TSS scattering are not influenced by the physical distance between the two interfaces film/vacuum and film/substrate. In contrast, the effective mass m^* at the Fermi wave vector k_F, being a property of the band structure, is affected by the presence of a gap $\Delta(L)$ at the Dirac point, and therefore for $L < 5$ QL depends on L. Hence,

$$\frac{\mu_t(L)}{\mu_t(L')} = \frac{m^*(L')}{m^*(L)} \tag{10}$$

holds. With Equation (2), the effective mass is given by[30]

$$m^*(L) = \hbar^2 k \left(\frac{dE}{dk}\right)^{-1}\Big|_{k=k_{F,t}}$$

$$= \hbar^2 k \left(2k(\hbar v_F)^2 \frac{1}{2\sqrt{[\hbar v_F k]^2 + [\Delta(L)/2]^2}}\right)^{-1}\Big|_{k=k_{F,t}}$$

$$= \frac{1}{v_F^2} \sqrt{E_{F,t}^2 + [\Delta(L)/2]^2} \tag{11}$$

The parametric dependence on $E_{F,t}$, which in turn may depend on L, is noted. Equation (3) follows directly from this equation. Setting $L' = 5$ QL in Equation (3), $\mu_t(L)$ for any $L < 5$ QL in terms of $\mu_t(5\,\text{QL})$ was calculated, which in turn is given by (Equation (1))

$$\mu_t(5\,\text{QL}) = \frac{\sigma(5\,\text{QL})}{e[n_t(5\,\text{QL}) + r_\mu n_b(5\,\text{QL})]} \tag{12}$$

where $\mu_b(L) = r_\mu \mu_t(L)$ was assumed, that is, a constant ratio between the mobilities in the top and bottom TSS. The resulting expression is

$$\mu_t(L) = v_F^2 \frac{\sigma(5\,\text{QL})}{e[n_t(5\,\text{QL}) + r_\mu n_b(5\,\text{QL})]} \frac{1}{\sqrt{E_{F,t}^2 + [\Delta(L)/2]^2}} \tag{13}$$

which can be inserted into Equation (1)

$$\sigma(L) = e\mu_t(L)[n_t(L) + r_\mu n_b(L)] \tag{14}$$

to calculate the sheet conductivity for each film thickness, only considering intra-TSS scattering (Figure 3b). The parameters $E_{F,t}$, $E_{F,b}$, and r_μ in this equation were varied in the ranges $[-50\,\text{meV}; 50\,\text{meV}]$ and $[0.3; 1]$, respectively, always finding sheet conductivities that were too large in comparison with the experiment.

Modeling the Surface Conductivity: Including Inter-TSS Scattering: The scattering between the top and bottom TSS is governed by Fermi's golden rule, that is,

$$\frac{1}{\tilde{\tau}_t} = \frac{2\pi}{\hbar} D(E_{F,t}) |V_{t\to b}|^2 \tag{15}$$

with an equivalent equation for $\tilde{\tau}_b$. Evidently, the modulus-squared matrix elements for the scattering from the top to the bottom ($|V_{t\to b}|^2$) and from the bottom to the top ($|V_{b\to t}|^2$) surfaces must be the same. The contribution of inter-TSS scattering to the mobility is given by

$$\tilde{\mu}_t(L) = \frac{e}{m^*(L, E_{F,t})} \tilde{\tau}_t \tag{16}$$

with an equivalent expression for $\tilde{\mu}_b$. Together, both expressions yield

$$\tilde{\mu}_b = \tilde{\mu}_t \frac{\tilde{\tau}_b}{\tilde{\tau}_t} \frac{m^*(L, E_{F,t})}{m^*(L, E_{F,b})}$$

$$= \tilde{\mu}_t \frac{D(E_{F,t})\sqrt{E_{F,t}^2 + [\Delta(L)/2]^2}}{D(E_{F,b})\sqrt{E_{F,b}^2 + [\Delta(L)/2]^2}} \tag{17}$$

Because of the increasing wave function overlap between the two TSS, it is expected that in thermodynamic equilibrium $E_{F,t}$ approaches $E_{F,b}$ as L decreases, such that because of Fermi's golden rule $\tilde{\tau}_t \to \tilde{\tau}_b$, and finally also $\tilde{\mu}_t \to \tilde{\mu}_b$. In this modeling, it was assumed $E_{F,t} = E_{F,b}$, $\tilde{\tau}_t = \tilde{\tau}_b$, and $\tilde{\mu}_t = \tilde{\mu}_b$ for all $L \leq 4$ QL.

Using Matthiesen's rule, the effective mobility of the top surface $\mu_{\text{eff},t}(L)$ including the two scattering mechanisms is given by Equation (4). An equivalent equation is found for $\mu_{\text{eff},b}(L)$. These expressions enter Equation (1) to obtain the sheet conductivity

$$\sigma(L) = e\left[n_t(L) \frac{\mu_t(L)\tilde{\mu}_t(L)}{\mu_t(L) + \tilde{\mu}_t(L)} + n_b(L) \frac{r_\mu \mu_t(L)\tilde{\mu}_t(L)}{r_\mu \mu_t(L) + \tilde{\mu}_t(L)}\right] \tag{18}$$

In this equation, $\mu_t(L)$ is identical to the one from the previous model. To obtain $\tilde{\mu}_t(L)$, the above formula, after inserting the experimental sheet conductivity σ for each film thickness, was solved. Since n_t, n_b, and μ_t depend parametrically on $E_{F,t}$ and $E_{F,b}$, $E_{F,t}$, $E_{F,b}$ were varied together with r_μ in order to find the range in which the effective mobility $\mu_{\text{eff},t}(L)$ of the top surface must lie. This range is shown in Figure 4.

Supporting Information

Supporting Information is available from the Wiley Online Library or from the author.

Acknowledgements

Conflict of Interest

The authors declare no conflict of interest.

Data Availability Statement

Raw data used to produce the figures in the main text and the Supporting Information are available at the Jülich DATA public repository under DOI 10.26165/JUELICH-DATA/NJJZPL.

Keywords

scanning tunneling microscopy, surface states, thin films, topological insulators

[1] H. Zhang, C.-X. Liu, X.-L. Qi, X. Dai, Z. Fang, S.-C. Zhang, *Nat. Phys.* **2009**, *5*, 438.

[2] Y. Xia, D. Qian, D. Hsieh, L. Wray, A. Pal, H.-H. Lin, A. Bansil, D. Grauer, Y. Hor, R. J. Cava, M. Z. Hasan, *Nat. Phys.* **2009**, *5*, 398.

[3] Y. L. Chen, J. G. Analytis, J.-H. Chu, Z. K. Liu, S.-K. Mo, X. L. Qi, H. J. Zhang, D. H. Lu, X. Dai, Z. Fang, S. C. Zhang, I. R. Fisher, Z. Hussain, Z.-X. Shen, *Science* **2009**, *325*, 178.

[4] D. Hsieh, Y. Xia, D. Qian, L. Wray, J. H. Dil, F. Meier, J. Osterwalder, L. Patthey, J. G Checkelsky, N. P Ong, A. Fedorov, H.-H. Lin, A. Bansil, D. Grauer, Y. Hor, R. J Cava, M. Z. Hasan, *Nature* **2009**, *460*, 1101.

[5] C.-Z. Chang, J. Zhang, X. Feng, J. Shen, Z. Zhang, M. Guo, K. Li, Y. Ou, P. Wei, L.-L. Wang, Z.-Q. Ji, Y. Feng, S. Ji, X. Chen, J. Jia, X. Dai, Z. Fang, S.-C. Zhang, K. He, Y. Wang, L. Lu, X.-C. Ma, Q.-K. Xue, *Science* **2013**, *340*, 167.

[6] X. Kou, S.-T. Guo, Y. Fan, L. Pan, M. Lang, Y. Jiang, Q. Shao, T. Nie, K. Murata, J. Tang, Y. Wang, L. He, T.-K. Lee, W.-L. Lee, K. L. Wang, *Phys. Rev. Lett.* **2014**, *113*, 137201.

[7] C.-Z. Chang, W. Zhao, D. Y. Kim, H. Zhang, B. A. Assaf, D. Heiman, S.-C. Zhang, C. Liu, M. H. W. Chan, J. S. Moodera, *Nat. Mater.* **2015**, *14*, 473.

[8] Y. Deng, Y. Yu, M. Z. Shi, Z. Guo, Z. Xu, J. Wang, X. H. Chen, Y. Zhang, *Science* **2020**, *367*, 895.

[9] C. Liu, Y. Wang, H. Li, Y. Li, J. Li, K. He, Y. Xu, J. Zhang, Y. Wang, *Nat. Mater.* **2020**, *19*, 522.

[10] P. Roushan, J. Seo, C. V. Parker, Y. S. Hor, D. Hsieh, D. Qian, A. Richardella, M. Z. Hasan, R. J. Cava, A. Yazdani, *Nature* **2009**, *460*, 1106.

[11] H.-Z. Lu, W.-Y. Shan, W. Yao, Q. Niu, S.-Q. Shen, *Phys. Rev. B* **2010**, *81*, 115407.

[12] C.-X. Liu, H. Zhang, B. Yan, X.-L. Qi, T. Frauenheim, X. Dai, Z. Fang, S.-C. Zhang, *Phys. Rev. B* **2010**, *81*, 041307.

[13] T. Förster, P. Krüger, M. Rohlfing, *Phys. Rev. B* **2015**, *92*, 201404.

[14] T. Förster, P. Krüger, M. Rohlfing, *Phys. Rev. B* **2016**, *93*, 205442.

[15] Y. Zhang, K. He, C.-Z. Chang, C.-L. Song, L.-L. Wang, X. Chen, J.-F. Jia, Z. Fang, X. Dai, W.-Y. Shan, S.-Q. Shen, Q. Niu, X.-L. Qi, S.-C. Zhang, X.-C. Ma, Q.-K. Xue, *Nat. Phys.* **2010**, *6*, 584.

[16] Y. Jiang, Y. Wang, M. Chen, Z. Li, C. Song, K. He, L. Wang, X. Chen, X. Ma, Q.-K. Xue, *Phys. Rev. Lett.* **2012**, *108*, 016401.

[17] T. Zhang, J. Ha, N. Levy, Y. Kuk, J. Stroscio, *Phys. Rev. Lett.* **2013**, *111*, 056803.

[18] S. Bauer, C. Bobisch, *Nat. Commun.* **2016**, *7*, 11381.

[19] F. Lüpke, M. Eschbach, T. Heider, M. Lanius, P. Schüffelgen, D. Rosenbach, N. Von Den Driesch, V. Cherepanov, G. Mussler, L. Plucinski, D. Grützmacher, C. Schneider, B. Voigtländer, *Nat. Commun.* **2017**, *8*, 15704.

[20] N. Fukui, R. Hobara, A. Takayama, R. Akiyama, T. Hirahara, S. Hasegawa, *Phys. Rev. B* **2020**, *102*, 115418.

[21] F. Lüpke, J. Sven, M. Eschbach, T. Heider, E. Mlynczak, M. Lanius, P. Schüffelgen, D. Rosenbach, N. v d Driesch, V. Cherepanov, G. Mussler, L. Plucinski, D. Grützmacher, C. M. Schneider, F. S. Tautz, B. Voigtländer, *npj Quantum Mater.* **2018**, *3*, 46.

[22] S. Just, F. Lüpke, V. Cherepanov, F. S. Tautz, B. Voigtländer, *Phys. Rev. B* **2020**, *101*, 245413.

[23] B. Skinner, T. Chen, B. I. Shklovskii, *J. Exp. Theor. Phys.* **2013**, *117*, 579.

[24] J. Kellner, M. Eschbach, J. Kampmeier, M. Lanius, E. Młyńczak, G. Mussler, B. Holländer, L. Plucinski, M. Liebmann, D. Grützmacher, C. M. Schneider, M. Morgenstern, *Appl. Phys. Lett.* **2015**, *107*, 251603.

[25] S. Bauer, A. M. Bernhart, C. A. Bobisch, *Appl. Surf. Sci.* **2018**, *432*, 140.

[26] A. Leis, M. Schleenvoigt, A. Jalil, V. Cherepanov, G. Mussler, D. Grützmacher, F. Tautz, B. Voigtländer, *Sci. Rep.* **2020**, *10*, 2816.

[27] B. Voigtländer, V. Cherepanov, S. Korte, A. Leis, D. Cuma, S. Just, F. Lüpke, *Rev. Sci. Instrum.* **2018**, *89*, 101101.

[28] I. Miccoli, F. Edler, H. Pfnür, C. Tegenkamp, *J. Phys.: Condens. Matter* **2015**, *27*, 223201.

[29] J. Zhang, C.-Z. Chang, Z. Zhang, J. Wen, X. Feng, K. Li, M. Liu, K. He, L. Wang, X. Chen, Q.-K. Xue, X. Ma, Y. Wang, *Nat. Commun.* **2011**, *2*, 574.

[30] V. Ariel, A. Natan, Electron Effective Mass in Graphene, arXiv:1206.6100 (https://arxiv.org/abs/1206.6100), **2012**.